First-principles study of substitutional metal impurities in graphene: structural, electronic and magnetic properties

2010 New J. Phys. 12 053012

(http://iopscience.iop.org/1367-2630/12/5/053012)

New Journal of Physics
The open-access journal for physics

First-principles study of substitutional metal impurities in graphene: structural, electronic and magnetic properties

E J G Santos, A Ayuela and D Sánchez-Portal[1]

Centro de Física de Materiales CSIC-UPV/EHU—Materials Physics Center (MPC), Paseo Manuel de Lardizabal 5, 20018 San Sebastián, Spain
and
Donostia International Physics Center (DIPC), Paseo Manuel de Lardizabal 4, 20018 San Sebastián, Spain
E-mail: eltonjose_gomes@ehu.es, swxayfea@ehu.es and sqbsapod@ehu.es

New Journal of Physics **12** (2010) 053012 (32pp)
Received 27 November 2009
Published 7 May 2010
Online at http://www.njp.org/
doi:10.1088/1367-2630/12/5/053012

Abstract. We present a theoretical study using density functional calculations of the structural, electronic and magnetic properties of 3d transition metal, noble metal and Zn atoms interacting with carbon monovacancies in graphene. We pay special attention to the electronic and magnetic properties of these substitutional impurities and find that they can be fully understood using a simple model based on the hybridization between the states of the metal atom, particularly the d shell, and the defect levels associated with an unreconstructed D_{3h} carbon vacancy. We identify three different regimes associated with the occupation of different carbon–metal hybridized electronic levels: (i) bonding states are completely filled for Sc and Ti, and these impurities are non-magnetic; (ii) the non-bonding d shell is partially occupied for V, Cr and Mn and, correspondingly, these impurities present large and localized spin moments; (iii) antibonding states with increasing carbon character are progressively filled for Co, Ni, the noble metals and Zn. The spin moments of these impurities oscillate between 0 and $1\mu_B$ and are increasingly delocalized. The substitutional Zn suffers a Jahn–Teller-like distortion from the C_{3v} symmetry and, as a consequence, has a zero spin moment. Fe occupies a distinct position at the border between regimes (ii) and (iii) and shows a more complex behavior: while it is non-magnetic at

[1] Author to whom any correspondence should be addressed.

the level of generalized gradient approximation (GGA) calculations, its spin moment can be switched on using GGA + U calculations with moderate values of the U parameter.

Contents

1. Introduction

The electronic properties of two-dimensional graphene are currently the subject of intense experimental and theoretical research [1, 2]. Graphene exhibits many intriguing phenomena stemming from the characteristic conical dispersion and chiral behavior of its valence and conduction bands near the Fermi energy [3]–[5]. In general, graphenic nanostructures such as graphene nanoribbons, carbon nanotubes and their interconnections are opening new routes for research in the field of nanoelectronics [6]. In particular, carbon-based materials are quite promising for spintronics and related applications due to their long spin relaxation and decoherence times owing to the low intrinsic spin–orbit interaction and the low hyperfine interaction of the electron spins with the carbon nuclei [7]–[11]. Furthermore, the possibility of controlling the magnetism of edge states in nanoribbons and nanotubes by applying external electric fields introduces an additional degree of freedom to controlling the spin transport [12]–[14]. However, for the design of realistic devices, the effects of defects and impurities have to be taken into account. For this reason, much work has been devoted to the study of defects and different types of impurities in these materials. It has now become clear that defects and dopants severely affect some of the properties of graphenic systems and can be

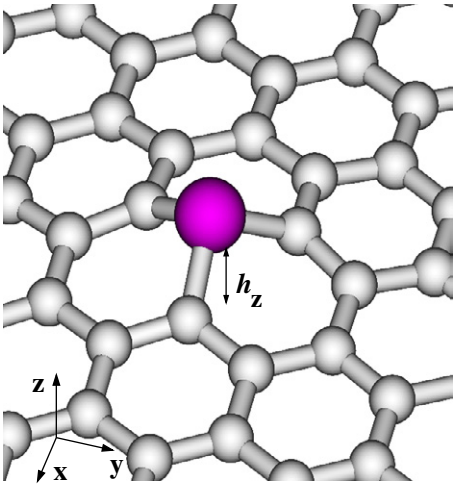

Figure 1. Typical geometry of transition and noble substitutional metal atoms in graphene. The metal atom moves upwards from the layer and occupies, in most cases, an almost perfectly symmetric threefold position with C_{3v} symmetry.

used to tune their response. For example, the strong interplay between the presence of defects or dopants and the magnetic properties of carbon nanostructures has been stressed by several authors [15]–[23].

Here we focus on substitutional impurities in graphene, in which a single metal atom substitutes one or several carbon atoms in the layer. Direct experimental evidence for the existence of this kind of defect has been recently provided by Gan *et al* [24]. Using high-resolution transmission electron microscopy (HRTEM), these authors were able to visualize individual Au and Pt atoms incorporated into a very thin graphitic layer probably consisting of one or two graphene layers. From the real-time evolution and temperature dependence of the dynamics, they obtained information about the diffusion of these atoms. Large diffusion barriers (∼2.5 eV) were observed for in-plane migration, which indicates the high stability of these defects and the presence of strong carbon–metal bonds. These observations seem to indicate that the atoms occupy substitutional positions. Evidence also exists of the existence of substitutional Ni impurities in single-walled carbon nanotubes (SWCNT) [25, 26] and graphitic particles [27]. Ushiro *et al* [25] showed that Ni substitutional defects were present in SWCNT samples even after careful purification and that, according to their analysis of the x-ray absorption data, the most likely configuration was the one in which the Ni atom replaces a carbon atom, similar to that shown in figure 1.

The presence of substitutional defects can have important implications for the interpretation of some experimental evidence. For example, substitutionals of magnetic transition metals are expected to strongly influence the magnetic properties of graphenic nanostructures. Interestingly, transition metals like Fe, Ni or Co are among the most common catalysts used for the production of SWCNT [28]. Furthermore, Rodriguez-Manzo and Banhart [29] recently demonstrated the possibility of creating individual vacancies at desired locations in carbon nanotubes using electron beams. This ability, combined with the observed stability of substitutional impurities, can open a route to the fabrication of new devices incorporating substitutional impurities in certain locations or arranged in particular ways. Such devices would allow for experimental verification of some of the unusual magnetic interactions mediated by the graphenic carbon network that have been predicted recently [30]–[32].

In this work, we study theoretically the structural, electronic and magnetic properties of 3d transition metals, noble metals and Zn as substitutional impurities in graphene using density functional (DFT) calculations. We only consider the configuration proposed by Ushiro *et al* [25] in which a single metal atom binds to a carbon monovacancy. Throughout the paper we will refer to this structure as the substitutional configuration. The results of our DFT calculations are in good agreement with the results of other recent studies on similar systems [26], [32]–[36]. In particular, Krasheninnikov *et al* [33] presented the most complete first-principles study to date of metal atoms interacting with single and double vacancies in graphene. In most cases our results are in good agreement with their predictions and similar general trends are found. However, the electronic structure of these defects has not been analyzed in detail to date and no simple model for understanding the observed behaviors has been presented so far. Here we present the evolution of the electronic structure of the substitutional defects as we move along the transition series and correlate the observed changes with a simple picture of the metal–vacancy interaction.

In our study we pay special attention to the electronic and magnetic properties of the metal impurities. One of our key results is that the electronic and magnetic properties of these substitutional metals can be fully understood using a simple model based on the hybridization between the states of the metal atom, particularly the d shell, and the defect levels associated with the unreconstructed carbon vacancy. The predictions of this model are in good agreement with the calculated DFT band structures. Using this model we can easily understand the non-trivial behavior found for the binding energy and for the size and localization of the spin moment as we increase the number of valence electrons in the impurity. Briefly, we have identified three different regimes that can be correlated with the electron filling of different carbon–metal hybridized levels: (i) bonding states are filled for Sc and Ti, and these impurities are non-magnetic; (ii) the non-bonding d shell is partially occupied for V, Cr and Mn and, correspondingly, these impurities present large and localized spin moments; (iii) antibonding states with increasing carbon character are progressively filled for Co, Ni, the noble metals and Zn, giving rise to spin moments that oscillate between 0 and 1 μ_B and are increasingly delocalized.

We have also found that Zn becomes non-magnetic due to a Jahn–Teller distortion. However, it is possible to stabilize a symmetric configuration with a spin moment of $2\mu_B$ with a very small energy penalty of $\sim$150 meV. Finally, our calculations confirm that the unexpected result that Au substitutionals [33, 34] present a spin moment of 1 μ_B also holds for Ag and Cu and thus stems only from the number of valence electrons (see the Slater–Pauling-like plot in figure 3).

We have studied in detail the complex case of Fe. This impurity occupies a distinct position at the boundary between two different regimes and its magnetic behavior stems from the competition between the carbon–metal hybridization and the electron–electron interaction within the 3d shell. As a result, the spin moment of Fe is especially difficult to describe: although non-magnetic using standard functionals within the generalized gradient approximation (GGA) [37], the magnetism of Fe appears using the so-called LDA + U methodology with reasonably low values of the U parameter. The difficulties in describing the magnetism of Fe also manifest themselves in the recent work by Venezuela *et al* [38]. These authors have shown that the existence of localized spin moments associated with Fe substitutionals can depend critically on the particular magnetic order imposed on an array of such defects and thus on the use of periodic boundary conditions.

The paper is organized as follows. After a brief description of the computational approach in section 2, we present a summary of the structure, energetics and magnetic properties of all the elements studied in section 3. In this section, we also indicate the general ideas behind our model of the metal–carbon hybridization in these systems. In section 4, the electronic structure of the unreconstructed D_{3h} carbon vacancy in graphene is presented. This is one of the key ingredients to understanding the binding and electronic structure of substitutional impurities in graphene. The electronic structure of the different groups of impurities is described in the subsequent sections, particularly in section 5. The Zn substitutional impurity with its Jahn–Teller distortion is described in section 6. A section (section 7) is devoted to describing the special role of Fe at the border between two different regimes. Finally, we close with some general conclusions.

2. Theoretical methods

We have used two different approaches to perform our DFT calculations: the SIESTA method [39]–[41] using a basis set of localized numerical atomic orbitals (NAOs) [40, 42] and the VASP code [43, 44] using a basis set of plane waves. We have used the Perdew–Burke–Ernzerhof [37] GGA (PBE-GGA) functional in all our calculations. Most of our results are obtained using a 4×4 supercell. This supercell is sufficiently large to obtain reliable results. This has been proven by performing calculations using larger supercells up to 8×8 for several elements. The codes utilized perform three-dimensional periodic calculations. In order to avoid spurious interactions between periodic images of the defective graphene layer, the size of the supercell perpendicular to the plane was always larger than 15 Å. The convergence with respect to the number of k-points was especially critical to obtaining accurate results for the spin moment in the systems studied. For all the impurities and different supercell sizes, we used a large number of k-points, consistent with a 136×136 Monkhorst–Pack [45] sampling of the unit cell of graphene, in combination with a Fermi smearing of 21 meV. All the atomic coordinates were always optimized until forces in all directions were smaller than 0.05 eV $Å^{-1}$.

For the SIESTA calculations, we used Troullier–Martins norm-conserving pseudopotentials [46] generated using the pseudization radii shown in the appendix. The pseudopotentials for the metal atoms include nonlinear core corrections [47] for exchange and correlation. The pseudocore radii (r_{core}) have been optimized for each element and are also presented in the appendix. Using nonlinear core corrections is known to be critical to describe properly the spin moment and magnetic properties of transition metals. We tested that these pseudopotentials yield the correct spin moments and band structures in bulk phases.

The spacing of the real-space grid used to calculate the Hartree and exchange-correlation contribution to the total energy and Hamiltonian with SIESTA was equivalent to a 180 Ry plane-wave cutoff. A double-ζ polarized (DZP) [40, 42] basis set was used for the calculation of the magnetic and electronic properties. However, we checked that using a double-ζ (DZ) basis set for carbon yields almost identical relaxed structures as the DZP basis and therefore we used the smaller DZ basis for most of the structural relaxations. The shape of the basis orbitals was automatically determined by SIESTA using the algorithms described in [40]. The cutoff radii of the different orbitals were obtained using an *energy shift* of 50 meV. Although this basis set proved to be sufficiently accurate for describing the geometries, spin moments and band structures, for some metal atoms the binding energies were slightly overestimated. For these atoms, the radii of the basis orbitals were enlarged (using smaller values of the *energy shift* parameter) until binding energies were converged within a few tens of meV. The resulting radii are shown in the appendix.

With the VASP code we have used a well-converged plane-wave cutoff energy of 400 eV combined with the projected-augmented wave (PAW) method. Using the provided PAW potentials allows us to check the possible limitations of pseudopotential calculations. However, as shown below, agreement between both the sets of calculations is excellent. We also performed GGA + U calculations using the formulation of Dudarev *et al* [48]. In this formulation a single U parameter is used, which we have taken as an empirical parameter and varied in the range 1–4.5 eV in our calculations for all the studied impurities. Only for Fe, GGA + U results showed significant (qualitative) differences with respect to the results of PBE-GGA calculations.

In a recent paper, Venezuela *et al* [38] questioned the use of the supercell approach to calculate the magnetic properties of defects in graphene. According to these authors, the use of periodic boundary conditions (that force a particular magnetic alignment) in combination with the very slow decay of magnetic interactions in low-dimensional systems like graphene can introduce spurious effects that affect the calculated value of the spin moment. In particular, these authors claim that Fe substitutional impurities in graphene were reported as non-magnetic in [33] due to this effect.

In order to check the importance of effects introduced by the periodic boundary conditions, we performed most of our calculations using two supercells of quite different sizes (4×4 and 8×8). In all cases, the results (including those of the spin moment) are almost identical using these two simulation cells. Although this does not rule out the effect described by Venezuela *et al* for the local spin moment, it clearly indicates that the geometries, adsorption energies and electronic band structures are well converged with the supercells used. In particular, we focus here on the description of the characteristics and energy positions of the defect levels and how they stem from the corresponding impurity levels of a single carbon vacancy. This information is only slightly affected by the use of the supercell approximation.

Furthermore, our analysis of the electronic structure helps us to understand and predict the different sensitivities of different substitutionals to the boundary conditions. For example, for V, Cr and Mn substitutionals the spin moment is due to the polarization of the localized non-bonding 3d levels and, thus, is quite robust and insensitive to the boundary conditions. This finding is in agreement with the results of Venezuela *et al* for Mn. In contradistinction the defect levels near the Fermi energy for Fe, Co and Ni impurities have a larger carbon component, are more delocalized and therefore can be more sensitive to the boundary conditions. However, we analyzed in detail the case of Co, and the spin moment of 1 μ_B is quite robust and survives except for configurations in which two Co impurities are located very close in different graphene sublattices [32]. The possibility of magnetic Ni substitutionals has already been ruled out by Venezuela *et al* using a Stoner-like criterion [38]. Therefore, Fe is singled out as a system at the border between developing or not developing a spin moment. This agrees fully with the results reported in the present paper, where we explicitly show that Fe substitutionals are quite close to becoming spin polarized. For instance, we will show that moderate geometric changes and/or moderate increments of the on-site Coulomb interactions are sufficient to create a spin moment for the, otherwise non-magnetic, Fe substitutionals.

3. The main properties of substitutional transition metals in graphene

In this section we provide a brief summary of our results for the structure, binding and spin moments of substitutional 3d transition metals, noble metals and Zn in graphene.

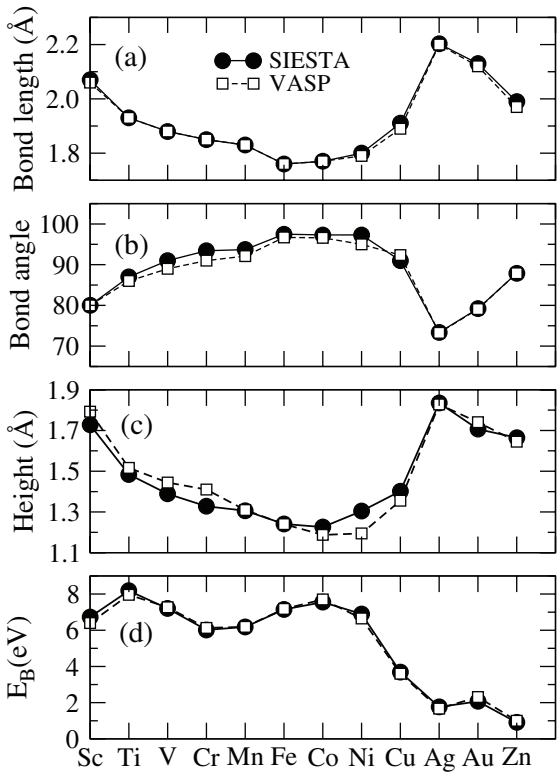

Figure 2. Structural parameters and binding energies of substitutional transition and noble metals in graphene. Bond lengths and angles have been averaged for the noble metals. The data presented for Zn correspond to the high-spin solution with C_{3v} symmetry and are very close to the averaged results for the most stable distorted solution.

3.1. Geometry and structural parameters

The typical geometry of the systems studied in this paper is presented in figure 1. The metal atom always appears displaced from the carbon layer. The height over the plane defined by its three nearest carbon neighbors is in the range 1.7–0.9 Å. These three carbon atoms are also displaced over the average position of the graphene layer by 0.3–0.5 Å. The total height (h_z) of the metal atom over the graphene plane is the sum of these two contributions and ranges between 1.2 and 1.8 Å, as shown in figure 2(c). In most cases, the metal atom occupies an almost perfect symmetric configuration with C_{3v} symmetry. Exceptions are the noble metals, which are slightly displaced from the central position, and Zn that suffers a Jahn–Teller distortion in its most stable configuration. However, we have found that it is also possible to stabilize a symmetric configuration for Zn with a binding energy only ∼150 meV smaller. This configuration was overlooked in a recently published study of these systems [33] and we will refer to it as $Zn_{C_{3v}}$ throughout the paper.

Figures 2 presents a summary of the structural parameters of substitutional 3d transition metals, noble metals and Zn in graphene. Solid circles correspond to calculations using the SIESTA code with pseudopotentials and a basis set of atomic orbitals, while open squares stand for VASP calculations using plane waves and PAW potentials. The agreement between both sets of calculations is quite remarkable. Data in these figures correspond to calculations using a

4×4 supercell of graphene. For several metals we also performed calculations using a larger 8×8 supercell and found almost identical results. This is particularly true for the total spin moments, which are less dependent on the size of the supercell, but require a sufficiently dense k-point sampling to converge. In the following we will mainly discuss the results obtained with the smaller cell since the plots of the band structures are easier to interpret in that case. Finally, as already mentioned, noble metals and Zn present a distorted configuration. A detailed description of the structural parameters in these cases will be given below; here we only present the averaged structural data for noble metals and those corresponding to the $Zn_{C_{3v}}$ case.

The data in figure 2 are basically consistent with those reported by Krasheninnikov *et al* in [33]. The behavior of the metal–carbon bond length and the height (h_z) of the impurity over the layer reflects approximately the size of the metal atom. For transition metals these distances decrease as we increase the atomic number, with a small discontinuity when going from Mn to Fe. The carbon–metal bond length reaches its minimum for Fe ($d_{C-Fe} = 1.76$ Å), keeping a very similar value for Co and Ni. For Cu and Zn the distances increase, reflecting the fully occupied 3d shell and the large size of the 4s orbitals. Among the noble metals we find that, as expected, the bond length largely increases for Ag with respect to Cu, but slightly decreases when going from Ag to Au. The latter behavior can be understood from the compression of the 6s shell due to scalar relativistic effects.

3.2. Binding energies

The binding energies of the substitutional metal atoms in graphene studied can be found in figure 2(d). In general, the behavior of the binding energies can be correlated with that of the carbon–metal bond length, although the former is somewhat more complicated. Binding energies for transition metals are in the range of 8–6 eV. Ti presents the maximum binding energy, which can be easily understood since for this element all the metal–carbon bonding states (see section 5.1) become fully occupied. One could expect a continuous decrease of the binding energy as we move away from Ti along the transition metal series, as first the non-bonding 3d and later the metal–carbon antibonding levels become populated. However, the behavior is non-monotonic and the smaller binding energies among the 3d transition metals are found for Cr and Mn, while a local maximum is observed for Co. This complex behavior is related to the simultaneous energy down-shift and compression of the 3d shell of the metal as we increase the atomic number. This will become more transparent when the metal–carbon hybridization levels are discussed in detail. In brief, the behavior of the binding energies of the substitutional 3d transition metal comes from two competing effects:

(i) as the 3d shell becomes occupied and moves to lower energies the hybridization with the carbon vacancy states near the Fermi energy (E_F) is reduced, which decreases the binding energy;

(ii) the transition from Mn to late transition metals is accompanied by a shift of the metal-carbon bond length of ∼0.1 Å, which increases the carbon–metal interaction and, correspondingly, the binding energy.

Binding energies for noble metals are considerably smaller than for transition metals and mirror the reverse behavior of the bond lengths: 3.69, 1.76 and 2.07 eV, respectively, for Cu, Ag and Au. The smallest binding energy (∼1 eV) among the metals studied here is found for Zn, with filled s–d electronic shells.

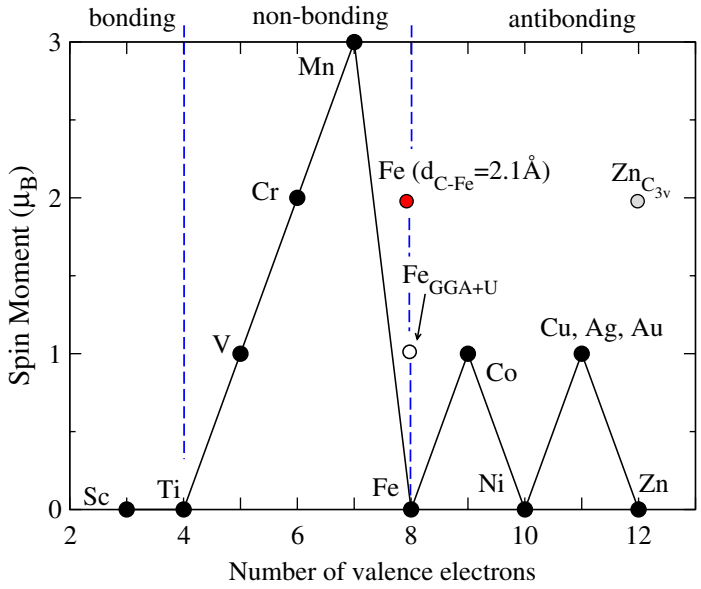

Figure 3. Spin moment of the substitutional transition and noble metals in graphene as a function of the number of valence electrons (Slater–Pauling-type plot). Black symbols correspond to the most stable configurations using GGA. Results are almost identical using SIESTA and VASP codes. Three main regimes are found as explained in detail in the text: (i) filling of the metal–carbon bonding states gives rise to the non-magnetic behavior of Ti and Sc; (ii) non-bonding d states are filled for V, Cr and Mn giving rise to high spin moments; (iii) for Fe all non-bonding levels are occupied and metal–carbon antibonding states start to be filled, giving rise to the observed oscillatory behavior for Co, Ni, Cu and Zn. Open and gray (red) symbols correspond, respectively, to calculations of Fe using GGA + U and artificially increasing the height of the metal atom over the graphene layer (see the text). The symbol marked as $Zn_{C_{3v}}$ corresponds to a Zn impurity in a high-spin symmetric C_{3v} configuration.

3.3. Spin moments

The spin moments of substitutional transition and noble metals in graphene are shown in figure 3. Again they are in agreement with the results of [33]. However, we advance a simple model for understanding the observed behavior which was not presented in that reference. One of the fundamental results of our study is a detailed model of the bonding and electronic structure of substitutional transition metals in graphene. As we will see below, the evolution of the spin moment can be completely understood using such a model. Briefly, we can distinguish different regimes according to the filling of electronic levels of different (bonding, non-bonding and antibonding) character:

(i) all the carbon–metal bonding levels are filled for Sc and Ti and, correspondingly, the spin moment is zero;

(ii) non-bonding 3d levels become populated for V and Cr, giving rise to a spin moment of, respectively, 1 and 2 μ_B with a strong localized d character;

Table 1. Mulliken population analysis of the spin moment in the central metal impurity (S_M) and the carbon nearest neighbors (S_C) for different substitutional impurities in graphene. S_{tot} is the total spin moment in the supercell.

	S_M (μ_B)	S_C (μ_B)	S_{tot} (μ_B)
V	1.21	−0.09	1.0
Cr	2.53	−0.20	2.0
Mn	2.91	−0.10	3.0
Co	0.44	0.06	1.0
Cu	0.24	−0.03, 0.31, 0.31	1.0
Ag	0.06	−0.31, 0.54, 0.54	1.0
Au	0.16	−0.28, 0.50, 0.50	1.0
$Zn_{C_{3v}}$	0.23	0.37	2.0

(iii) for Mn, one additional electron is added to the antibonding d_{z^2} level and the spin moment increases to 3 μ_B;

(iv) finally, for Fe and heavier atoms, all the non-bonding 3d levels are occupied and the spin moment oscillates between 0 and 1 μ_B as the antibonding metal–carbon levels become occupied.

The sudden decrease of the spin moment from 3 μ_B for Mn to 0 μ_B for Fe is characterized by a transition from a complete spin polarization of the non-bonding 3d levels to a full occupation of those bands. However, this effect depends on the ratio between the effective electron–electron interaction within the 3d shell and the metal–carbon interaction (see section 7). As we will see below, if the hybridization with the neighboring atoms is artificially reduced, for example by increasing the Fe–C distance, Fe impurities develop a spin moment of 2 μ_B. Our results show that it is also possible to switch on the spin moment of Fe by changing the effective electron–electron interaction within the 3d shell. This can be done using the so-called GGA + U method. For a large enough value of U (in the range 2–3 eV), Fe impurities develop a spin moment of 1 μ_B. This will be also explained in detail in section 7. For the time being, we just point out that this behavior is unique to Fe: using similar values of U for other impurities does not modify their spin moments.

At the level of the GGA calculations, Fe constitutes the border between two different characters of the spin moment associated with the substitutional metal impurities in graphene: 3d magnetism for V–Mn and a 'defective-carbon'-like magnetism for heavier atoms. For Co, Ni, the noble metals and Zn the electronic levels close to the E_F have a stronger contribution from the carbon nearest neighbors and resemble the levels of the isolated D_{3h} carbon vacancy. In particular, Mulliken population analysis shows that the spin moment of the noble metal impurities has a dominant contribution for the three nearest carbon neighbors (see table 1). For Zn, two electrons occupy a twofold degenerate level reminiscent of the E sp level of the unreconstructed carbon vacancy (see section 4). As a consequence, the system suffers a Jahn–Teller distortion and has a zero spin moment. However, it is possible to stabilize a symmetric configuration ($Zn_{C_{3v}}$) with a moment of 2 μ_B and only slightly higher in energy.

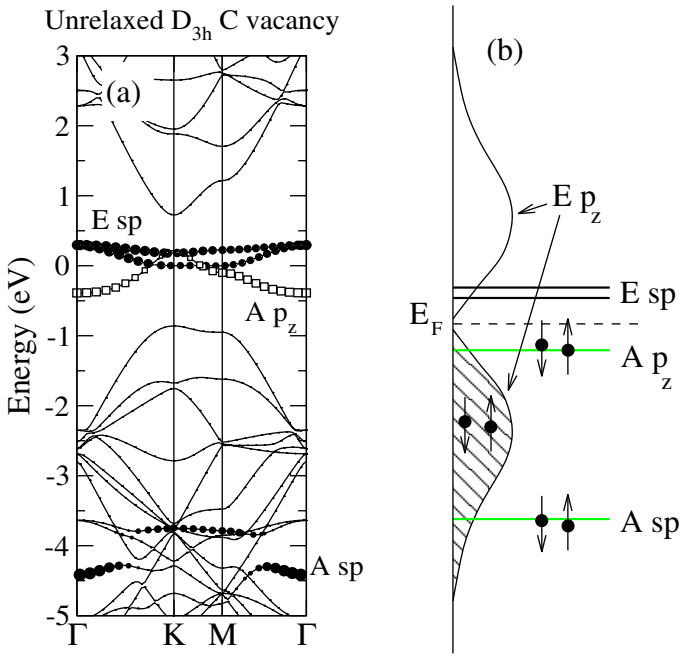

Figure 4. (a) Spin-compensated calculation of the band structure of an unrelaxed carbon vacancy (D_{3h} symmetry) in a 4×4 supercell of graphene. Symbols indicate those bands with larger weight on the carbon atoms around the vacancy (solid symbols for bands with sp character and open symbols for a band with p_z character). The electronic structure near E_F is dominated by a fully symmetric p_z level (A p_z) and two defect levels with E symmetry and sp character (E sp). Note that, due to the strong hybridization with the rest of the graphene layer, it is not possible to identify well-defined defect levels with E symmetry and p_z character. (b) Approximate scheme of the electronic structure of the spin-compensated D_{3h} C vacancy indicating the character and symmetry of the different levels and their occupations. The signal associated with the E p_z level extends over the whole valence and conduction bands.

4. Unreconstructed D_{3h} carbon vacancy

We have seen in the previous summary of results that, as substitutional impurities in graphene, most of the metal atoms studied here present a threefold symmetrical configuration. For this reason, we have found it particularly instructive to analyze their electronic structure as the result of hybridization between the atomic levels of the metal atoms with the electronic levels associated with an unrelaxed D_{3h} symmetrical carbon vacancy.

Figure 4(a) shows the electronic structure of a spin-compensated D_{3h} carbon vacancy as calculated using a 4×4 graphene supercell, while figure 4(b) presents a simplified scheme that highlights the defect levels associated with the vacancy and indicates their different character and symmetry. The actual D_{3h} vacancy shows a considerable spin polarization; however, here we only consider the spin-compensated case since the purpose of this calculation is to find the symmetries and approximate energy positions of the different energy levels. The defect levels of the D_{3h} vacancy can be easily classified according to their sp or p_z character and whether

they transform according to A or E-type representations. Close to the E_F we can find a fully symmetric A p_z level (thus belonging to the A_2'' irreducible representation) and two degenerate (at Γ) defect levels with E symmetry and sp character (E′ representation). Approximately 4 eV below E_F we find another defect level with A sp character (A_1' representation).

It is interesting to note that it is not possible to identify any localized defect level with E p_z (E″) character. This is due to the strong coupling with the delocalized states in the graphene layer and is in contrast to the case of the A p_z level. The A p_z level lies very close to E_F, where the density of states is low and, due to its A symmetry, cannot appreciably couple to the delocalized p_z states of graphene in that energy range. In contrast, the E p_z combinations present a very strong hybridization with the rest of the states of the graphene layer. Indeed, an inspection of the projected density of states (PDOS) (see the scheme in figure 4(b)) reveals that the spectral weight associated with such E-symmetry linear combinations of p_z orbitals of the carbon atoms surrounding the vacancy extends over the whole valence and conduction bands of graphene. It is important to take the last observation into account when developing a model of the electronic structure for the metal substitutionals in graphene. Note that we need to have the correct number of electrons from carbon available for forming localized (covalent) bonds.

The three carbon atoms around the vacancy provide three unpaired electrons associated with the unsaturated sp lobes and three electrons coming from the p_z orbitals. As shown in figure 4(b), two of these electrons stay in p_z states delocalized over the graphene layer, while the other four electrons fill the A sp and A p_z levels localized at the vacancy.

5. Analysis of the electronic structure

We now turn to the problem of the electronic structure of 3d transition and noble metal atoms as substitutional impurities in graphene. We first present a model of the hybridization between carbon and metal levels and, subsequently, we show that this model allows us to understand in detail the band structures obtained in our calculation for all the metals.

5.1. Sc and Ti: filling the vacancy–metal bonding levels

Figure 5(a) presents a schematic representation of the hybridization of the 3d levels of Ti with those of an unreconstructed D_{3h} carbon vacancy. We only consider explicitly the 3d states of the metal atom since our calculations show that, for transition metals, the main contribution from 4s orbitals appears well above E_F. Due to the symmetric position of the metal atom over the vacancy, the system has a C_{3v} symmetry and the electronic levels can still be classified according to the A or E irreducible representations of this point group. Of course, metal and carbon vacancy states only couple when they belong to the same irreducible representation. Thus, occupied A p_z and A sp vacancy levels can only hybridize with the $3d_{z^2}$ orbitals (A_1 representation), while all the other 3d metal orbitals can only couple to the unoccupied E sp vacancy levels.

With these simple rules in mind and taking into account the relative energy position of carbon and metal levels, which changes as we move along the transition metal series, we can propose a model of the electronic structure of substitutional transition metals in graphene as represented in figures 5(a) and (b). Some parameters in the model can be approximated from empirical information and/or simple calculations. For example, a rough estimate of the position of the 3d shell of the metal atom with respect to the graphene E_F can be obtained from the

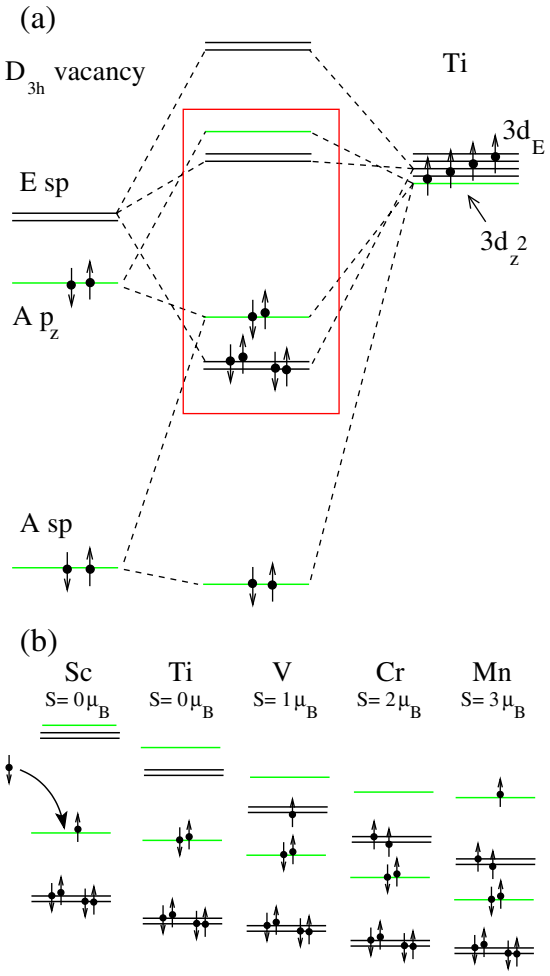

Figure 5. (a) Scheme of the hybridization between the 3d levels of Ti and the localized impurity levels of the D_{3h} C vacancy. Only d levels of Ti are represented since our calculations show that, at least for transition metals, the main contribution from s levels appears well above E_F. Levels with A symmetry are represented by gray (green) lines, while those with E symmetry are marked with black lines. The region close to E_F is highlighted by a (red) square. (b) Schematic representation of the evolution of the electronic structure near E_F for several substitutional transition metals in graphene. The spin moment (S) is also indicated. Substitutional Sc impurities act as electron acceptors, causing the p-doping of the graphene layer.

positions of the atomic levels, and the relative strengths of the different carbon–metal hoppings can be estimated from those of the corresponding overlaps. With such information it is already possible to obtain most of the features of the model in figure 5. However, some uncertainties remain, particularly concerning the relative positions of levels with different symmetry. To solve these uncertainties the simplest approach is to compare with our first-principles calculations and this is what we have done here. The details of the model presented in figure 5 have been obtained from a thorough analysis of our calculated band structures. In particular, we have used

the projection of the electronic states into orbitals of different symmetry as an instrumental tool to classify the levels and to obtain the rationale that finally guided us to the proposed model. However, it is interesting to note that some features that derive from our way of understanding the electronic structure of these defects are very robust and can actually be guessed without direct comparison with the calculated band structures. For example, the fact that for V we start to fill the non-bonding 3d states and, therefore, that this impurity, as well as Cr and Mn, develops a spin moment can be argued from simple symmetry and electron-counting arguments.

According to our model there are three localized defect levels with A_1 character and three twofold-degenerate levels with E character. Two of these E levels correspond to bonding–antibonding sp–d pairs, while the third one corresponds to 3d non-bonding states. For Sc–Mn the three A_1 levels can be pictured as a low-lying bonding level with A sp–d_{z^2} character and a bonding–antibonding pair with A p_z–d_{z^2} character.

Therefore, as shown in figure 5, we have four metal–vacancy bonding levels (two A and one doubly degenerate E levels) that can host up to eight electrons. Ti contributes with four valence electrons, and there are four electrons associated with the localized carbon–vacancy levels. Thus, for Ti the bonding states are completely occupied. Consequently, Ti presents the highest binding energy among all 3d transition metals and has a zero spin moment.

The situation for Sc ought to be discussed in detail. As Sc has three valence electrons, in principle we could expect an incomplete filling of the metal–vacancy bonding levels and a spin moment of $\sim 1\ \mu_B$. However, in our model, the highest bonding state (with A p_z–d_{z^2} character) appears below E_F and the Sc impurity can act as an acceptor impurity. Our calculations show that this is indeed the case. The Sc–vacancy p_z–d_{z^2} impurity level captures an electron from the extended states of the graphene layer, which becomes p-doped. In total, the substitutional Sc–graphene system does not show any spin polarization.

We can now contrast the expectations from our model with actual calculations. Figure 6 shows the band structure of (a) Sc and (b) Ti close to the E_F. As expected, the main contribution from the 3d shell is found above E_F. Below E_F we find one defect band with p_z–d_{z^2} character and two bands (degenerate at Γ) with sp–d character. These bands are in close correspondence with the bonding A and E levels appearing in our model. In the case of Ti the E_F is located inside a gap of ~ 0.5 eV that opens at K-point in the Brillouin zone. This gap appears due to the relatively small 4×4 supercell used in these calculations and is reduced when larger supercells are used. Thus, the filling of the graphene extended bands is not appreciably changed by substitutional doping with Ti. For Sc the situation is different. As shown in figure 6(a), E_F moves away from the K-point, the Sc–vacancy complex captures one electron and the graphene layer becomes doped with holes.

Regarding the unoccupied bands, the 3d contribution for Sc above E_F appears quite broadened due to the strong hybridization with the graphene states. Indeed, the defect levels are somewhat difficult to identify and to correlate with our model. One exception is a flat band with strong d_{z^2} character appearing at ~ 1.5 eV that, due to its symmetry, does not couple so efficiently with the host states. The case of Ti is much easier to interpret in terms of the simplified model presented in figure 5(a). In particular, we can find two bands at ~ 0.6 eV with strong d_{xy} and $d_{x^2-y^2}$ contribution that correspond to the non-bonding d impurity levels and one band with d_{z^2} character at ~ 0.8 eV corresponding to the A p_z–d_{z^2} antibonding level. Around 2.6 eV, we can also find the two E sp–d antibonding defect levels, although in this case much more hybridized with the host.

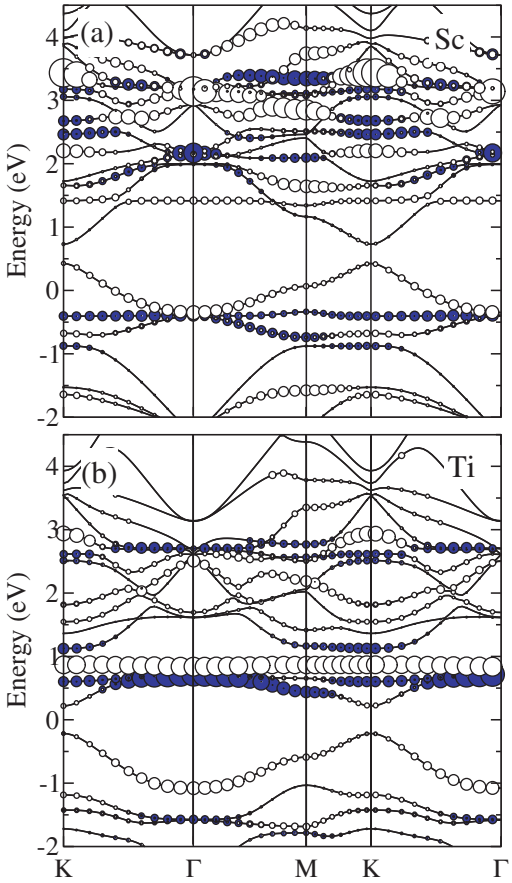

Figure 6. Calculated band structure of substitutional (a) Sc and (b) Ti impurities in a 4×4 supercell of graphene. Open circles indicate the contribution from $3d_{z^2}$ orbitals of the metal atom and C $2p_z$ orbitals of the neighboring C atoms. Solid circles indicate the contributions from the rest of the 3d orbitals and C $2p_x$ and $2p_y$ orbitals. Energies refer to the Fermi energy.

5.2. V, Cr and Mn: 3d magnetism

As we have seen above, the metal–vacancy bonding levels are completely filled for substitutional Sc and Ti and, as a consequence, the spin moment associated with these impurities is zero. However, following our model in figures 5(a) and (b), as we move along the transition metal series the number of valence electrons increases and the non-bonding 3d impurity states start to become occupied. Hence, due to the strong atomic character and localization of these states, the system develops a non-zero spin moment.

Figure 7 shows the calculated band structures for V, Cr and Mn impurities in a 4×4 supercell of graphene. The full calculations and the predictions of our simplified model agree remarkably, at least in the neighborhood of E_F. For V and Cr this correspondence is particularly evident: one and two electrons, respectively, occupy the degenerate non-bonding E d levels. These non-bonding levels have a dominant contribution from the $3d_{xy}$ and $3d_{x^2-y^2}$ orbitals of the metal atoms. As expected, the spin moments associated with these impurities are, respectively, 1 and $2\,\mu_B$. The strongly localized character of these spin moments is corroborated by the

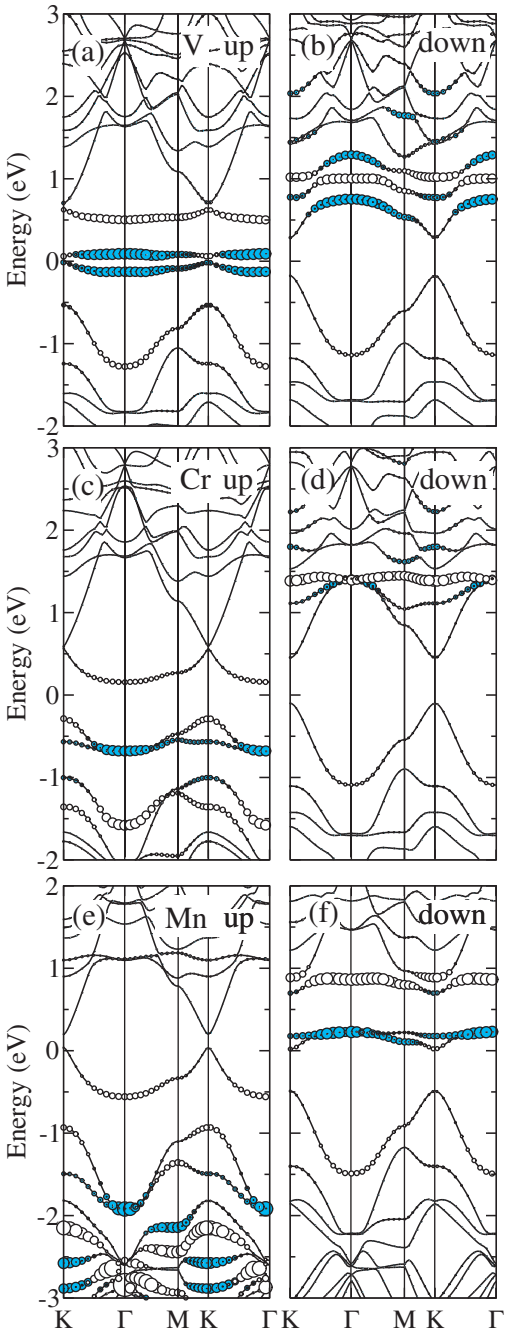

Figure 7. Calculated band structure of substitutional V ((a) and (b)), Cr ((c) and (d)) and Mn ((e) and (f)) impurities in a 4×4 supercell of graphene. Open and filled circles indicate, respectively, the contribution from $3d_{z^2}$ and the rest of the 3d orbitals of the metal and, therefore, also indicates levels with A and E symmetries. Energies refer to the Fermi energy.

Mulliken population analysis shown in table 1. This analysis indicates that the spin moment is mainly localized at the metal impurity. The contribution from the neighboring carbon atoms is much smaller and has the opposite sign. The localized character of the moment is also consistent

with the relatively large values of the spin splitting of the impurity bands. From figure 7, we calculate a spin splitting of ∼0.9 eV for V and almost 2 eV for Cr for the E d levels at E_F. These splittings are comparable to those of d-electrons in magnetic bulks, of the order of 1 eV.

Figures 7(e) and (f) show the majority and minority spin band structures for Mn substitutionals in graphene. In addition to the non-bonding 3d levels, the antibonding A p_z–d_{z^2} defect level also becomes occupied and spin polarized. This level has an important contribution from the $3d_{z^2}$ state of Mn (given by open symbols). Therefore, it is relatively localized within the Mn atom and presents a significant tendency towards spin polarization. Indeed, our calculations show that Mn substitutions in graphene give rise to a spin moment of $3\,\mu_B$. The Mulliken decomposition for Mn in table 1 again confirms the localized character of this spin moment. However, some differences with respect to V and Cr are also found. In those cases, the moment associated with the metal atoms was always larger that the total moment and the only significant additional contributions came from the nearest carbon neighbors. However, for Mn the atomic moment is somewhat smaller (2.91) than the total moment (3.0). Taking into account the contribution from the nearest carbon neighbors (−0.3), a moment of $\sim 0.4\mu_B$ is assigned to carbon atoms that are further away from the defect. This indicates a slightly more delocalized character of the spin moment of Mn, since for V and Cr the 'long range' contribution was smaller than $0.1\mu_B$. From the band structures in figures 7(e) and (f), we obtain a spin splitting of ∼2.1 eV for the non-bonding d levels of the Mn impurity, similar to the case of Cr. The spin splitting for the antibonding A p_z–d_{z^2} state has a smaller value of ∼1.5 eV, indicative of its larger spatial extension.

From the simple scheme presented in figure 5(a), we cannot completely determine the value of the spin moment of the Mn impurity. It can be $3\mu_B$ as found in our first-principles calculations and schematically depicted in figure 5(b). However, a magnetic moment of $1\mu_B$ is also a possible answer. In the latter case, the additional electron in Mn with respect to Cr could populate one of the minority-spin non-bonding d impurity levels instead of the antibonding A p_z–d_{z^2} level. In such a situation, the spin moment is determined by a delicate balance between the on-site exchange energy within the 3d shell and the energy cost ($\Delta\epsilon_{Ad}$) to promote one electron from the non-bonding d levels to the higher energy antibonding A p_z–d_{z^2} state. Note that the electron–electron repulsion is also reduced when the electron moves into the less localized A p_z–d_{z^2} level. An estimate of the exchange energy can be obtained from the spin splitting (Δ_S) of the defect levels near E_F. The relative position of the 3d states with respect to the A p_z level of the carbon vacancy and the interaction matrix element between these levels determine $\Delta\epsilon_{Ad}$. Thus, within our GGA-DFT calculations, we can expect the high-spin solution to be favored approximately when $\Delta_S > \Delta\epsilon_{Ad}$. From the band structures in figures 7(e) and (f), we obtain $\Delta\epsilon_{Ad} \sim 1.0$ eV, which is smaller than the values of Δ_S discussed previously and is therefore consistent with the calculated moment of $3\,\mu_B$ for Mn. Fe impurities considered below in detail present a similar situation where two spin configurations are possible. However, in the case of Fe, the low-spin (spin compensated) solution is preferred at the level of DFT-GGA calculations as a result of the stronger metal–carbon hybridization.

In short, both the results of the calculations and the expectations based on our model of the metal–vacancy bonding point toward a very strong 3d character of the defect levels appearing near E_F for V, Cr and Mn substitutional impurities in graphene. The filling of these localized levels favors high-spin solutions in accordance with the first Hund's rule of atomic physics. Thus, we can picture the appearance of spin polarization for V, Cr and Mn substitutionals in graphene as 'standard' d-shell magnetism.

5.3. Fe, Co, Ni: strong contribution from the carbon vacancy levels

As we have seen in the previous section, the defect levels appearing in the neighborhood of E_F associated with the presence of V, Cr and Mn substitutional impurities in graphene have a strong 3d character. Consequently, these impurities exhibit large spin moments. However, when increasing the atomic number along the transition series, the atomic 3d levels move to lower energies and we enter a different regime: the defect states near E_F have a predominant contribution from the carbon atoms neighboring the metal impurity. For 3d late transition metals heavier than Fe, noble metals and Zn, we can establish a strong link between the electronic structure of these impurities around E_F and that of the unreconstructed D_{3h} carbon vacancy.

A detailed scheme of the hybridization of Ni 3d states with those of the carbon vacancy, and the resulting electronic structure, is presented in figure 8(a). All the bonding and non-bonding metal–vacancy states are filled in this case and the levels appearing closer to E_F have antibonding character and a strong contribution from the three-carbon nearest neighbors. Closely below E_F we find a level with A character and a strong C $2p_z$ contribution and a smaller weight in the Ni $3d_{z^2}$ state. Above E_F there are two degenerate levels with E character mainly coming from the C 2sp lobes and hybridized with the Ni $3d_{xz}$ and $3d_{yz}$ orbitals. The resulting electronic structure strongly resembles that of the isolated D_{3h} (unreconstructed) carbon vacancy as can be checked by comparing the band structures in figures 4(a) and 9(d). The main difference stems from the slightly higher position of the unoccupied E levels in the case of the Ni impurity. This upward shift is due to the antibonding interaction with the d states of Ni and contributes to the stability of the C_{3v} spin-compensated solution. In the case of the D_{3h} carbon vacancy, the EC 2sp levels lie closer to E_F and make the system unstable against spin and structural distortions. This clear connection between the electronic structure of Ni and that of the D_{3h} vacancy was already emphasized in [26].

Thus, our GGA calculations predict Ni substitutional to be a closed shell system with zero spin moment. One could expect that a better description of the electron–electron interaction within the 3d shell would enhance any tendency of the system towards a magnetic instability. For this reason we have performed GGA + U calculations (using the VASP code) with values of U up to 4.5 eV. However, Ni substitutional impurities in *flat* graphene always remain non-magnetic in the calculations.

In [26], we proposed a different way of switching on the magnetism of Ni substitutionals: the possibility of spin moments induced by curvature. The idea consists of lifting the degeneracy of the two unoccupied E sp–d levels by applying a structural distortion. If the distortion is large enough, one of these levels close to E_F becomes partially populated and, due to its small bandwidth, spin polarized. We have checked that the curvature of the carbon layer in (n,n) nanotubes with n ranging between 4 and 8 induces spin moments as large as $0.8\mu_B$ per Ni substitutional impurity. The spin moment in these substitutionally Ni-doped nanotubes is strongly dependent, not only on the layer curvature, but on the density and arrangement of defects in the tube. We have recently demonstrated that a similar switching of the magnetic moment can be obtained in flat Ni-doped graphene by applying adequate structural distortions, thus providing a simple way of controlling the spin of this system [49].

As suggested by our scheme in figure 8(b), we can now try to understand the electronic structure of Co and Fe impurities from that of the Ni substitutional but removing, respectively, one and two electrons. According to this image, Co substitutionals should present a spin moment of 1 μ_B, while Fe substitutionals should be non-magnetic. This is indeed confirmed by our GGA calculations.

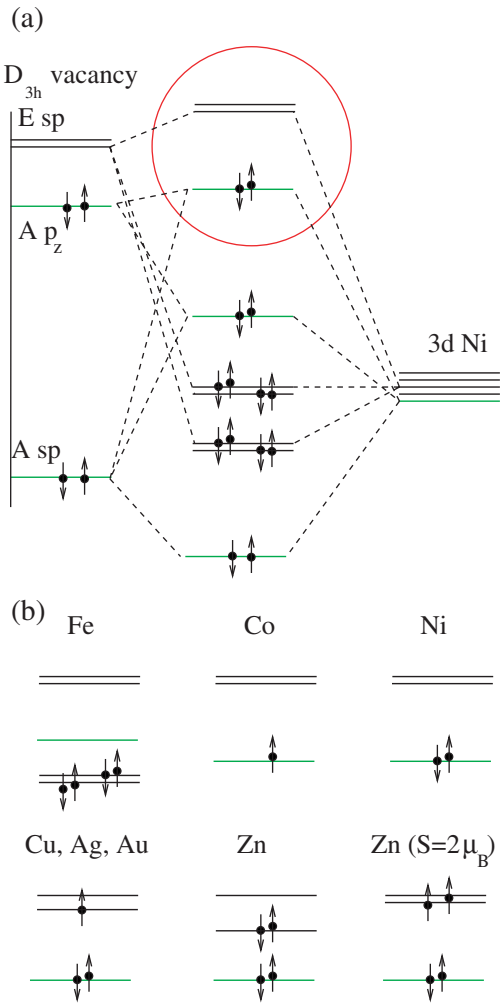

Figure 8. (a) Similar to figure 5(a) but for the case of Ni. The region close to the Fermi level is indicated by a (red) circle. (b) Scheme of the levels close to E_F for Fe, Co, Ni, noble metals and Zn. For Fe, in addition to the antibonding metal–vacancy levels, we have also included the non-bonding d levels that also appear quite close to E_F. The noble metals slightly break the C_{3v} symmetry. For Zn there are two solutions: a high spin solution that preserves symmetry and a distorted one with zero spin moment.

Figures 9(b) and (c) show, respectively, the majority and minority spin band structures of the Co impurity. In the neighborhood of E_F, we find a spin-polarized band associated with the antibonding A p_z–d_{z^2} impurity level. The spin splitting of this band is ∼0.5 eV. The hybridization character of this level is confirmed by the Mulliken analysis in table 1. Only a contribution of 0.44 μ_B to the total spin moment comes from the Co atom. The relatively delocalized character of the A p_z–d_{z^2} level also becomes evident. Only a moment of 0.18 μ_B comes from the three-carbon nearest neighbors, while 0.38 μ_B comes from carbon atoms at larger distances. The slow distance decay of the A p_z–d_{z^2} defect level translates into quite strong and long-range magnetic interactions between moments associated with neighboring

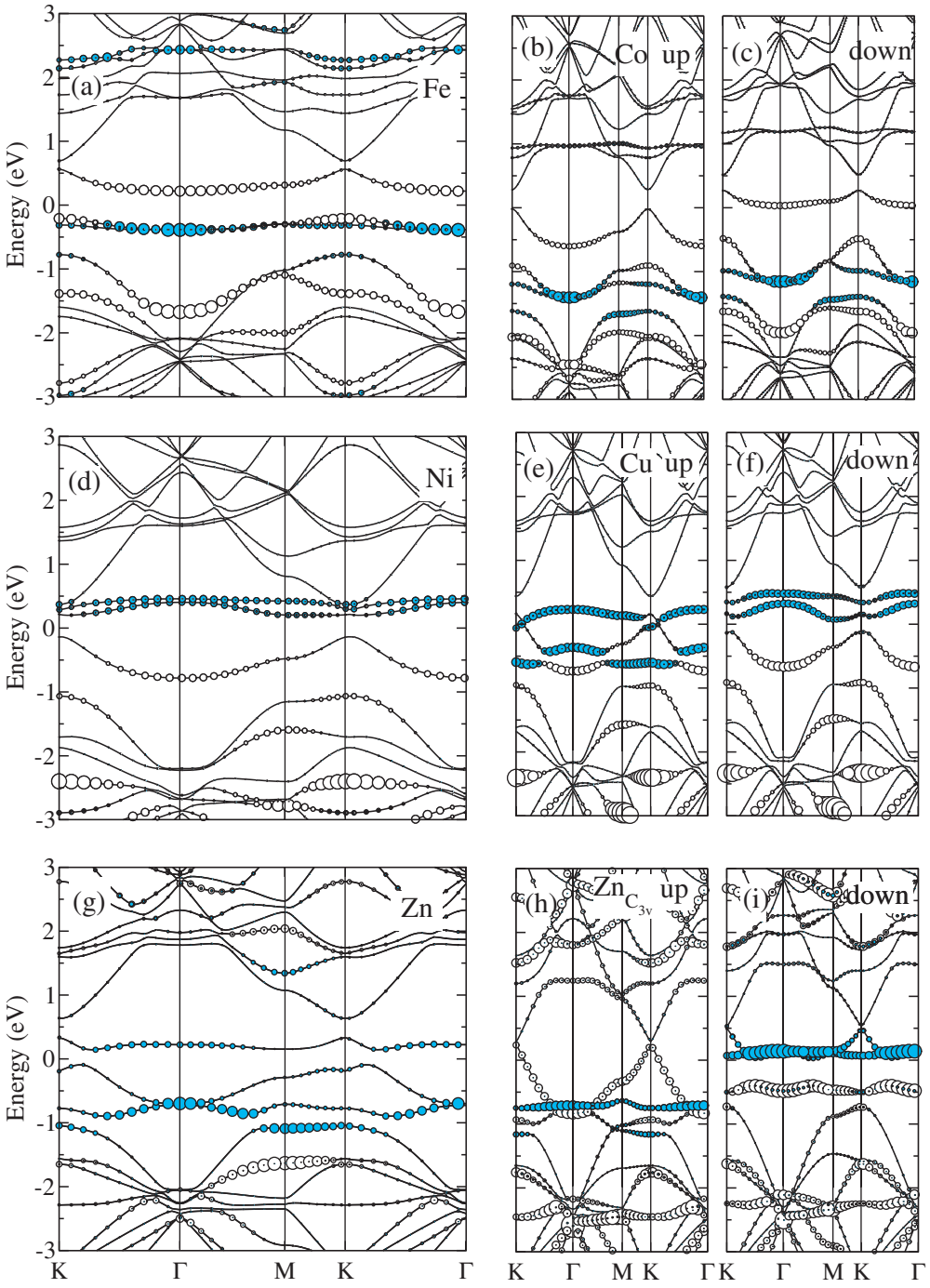

Figure 9. Similar to figure 7 but for Fe (a), Co ((b) and (c)), Ni (d), Cu ((e) and (f)), Zn (g) and symmetric $Zn_{C_{3v}}$ ((h) and (i)) substitutional impurities in graphene.

Co defects [32]. Indeed, the peculiar electronic structure of the Co impurities has important consequences for the magnetism of this system: couplings show a complex dependence with distance and direction, while the total spin moment is determined by the number of Co substitutions in each sublattice of the graphene layer. We refer the interested reader to [32].

Figure 9(a) presents the GGA band structure for an Fe substitutional defect in a 4×4 supercell of graphene. Similar results are found using a larger 8×8 supercell. This band structure is again in reasonable agreement with the simple model presented in figure 8. The non-bonding d levels are completely filled and appear $\sim$0.4 eV below E_F in the vicinity of Γ. The A p_z–d_{z^2} level is mostly unoccupied and close to 0.2 eV above E_F near Γ. However, we can see that near the K-point the p_z–d_{z^2} band becomes partially occupied, indicating a small charge transfer from the dispersive π bands of graphene to the defect. Mulliken analysis also reflects a small charge accumulation of $\sim$0.16 electrons in Fe. In spite of this small partial population, the spin-compensated solution is the most stable for Fe substitutionals at the GGA level.

As already pointed out in section 3.3, the magnetic behavior of the Fe impurity is the consequence of a delicate balance between the on-site electron–electron interaction and the metal–carbon hybridization. For this reason, we devote a whole section (section 7) to explore how the band structure and spin moment of Fe substitutionals are modified when these factors are independently controlled by changing the Fe–C bond length and using the GGA + U approximation to describe the effects of the electron–electron repulsion within the d-shell.

5.4. Noble metals

In the previous sections, we have seen that some of the traditional ferromagnets, like Fe and Ni, become non-magnetic as substitutional impurities in graphene. Also quite surprisingly, we find here that substitutional impurities of noble metals are magnetic with a spin moment of 1 μ_B. The reason for this behavior becomes clear once the electronic structure of these defects is understood.

The band structures can be found in figures 9(e) and (f) for Cu and in figure 10 for Ag and Au. In agreement with the predictions of our simplified model in figure 8, we can see that in the case of the noble–metal impurities the twofold degenerate E sp–d antibonding levels[2] are now occupied with one electron. The system undergoes a small structural distortion that removes the degeneracy of these levels and the unpaired electron becomes spin polarized. Therefore, substitutional impurities of the noble metals in graphene exhibit a spin moment of 1 μ_B. Relativistic effects are known to be much more important for Au than for Ag and Cu. Although we have not included spin–orbit coupling in our calculations, scalar relativistic effects are taken into account in the construction of the pseudopotentials. However, the similarities between the electronic structure of all three noble metals are evident, which indicates that bonding and magnetic behavior are mainly dictated by the number of valence electrons.

Structural parameters for all noble metal impurities can be found in table 2. For Cu and Ag one of the metal–carbon bond lengths is slightly larger than the other two, whereas for Au one is shorter than the other. However, the distortions are rather small with variations of the bond lengths smaller than 2%. The differences introduced by the larger scalar relativistic effects of Au mainly reflect in the slightly smaller metal–carbon bond length for this metal as compared with Ag.

[2] For simplicity and consistency we use, throughout the paper, the same nomenclature to label the different defect levels. However, it should be understood that for the noble metals and Zn, the so-called antibonding A p_z–d_{z^2} level presents a sizeable contribution from the metal s orbital, while the degenerate E sp–d levels have non-negligible contributions from the p orbitals of the metal.

Table 2. Structural parameters for substitutional noble metals in graphene.

	d_{C-M} (Å)	h_z (Å)	θ (°)
Cu	1.93, 1.90, 1.90	1.40	88.9, 88.9, 95.2
Ag	2.23, 2.19, 2.19	1.84	71.7, 71.7, 76.7
Au	2.09, 2.12, 2.12	1.71	78.0, 78.0, 81.6

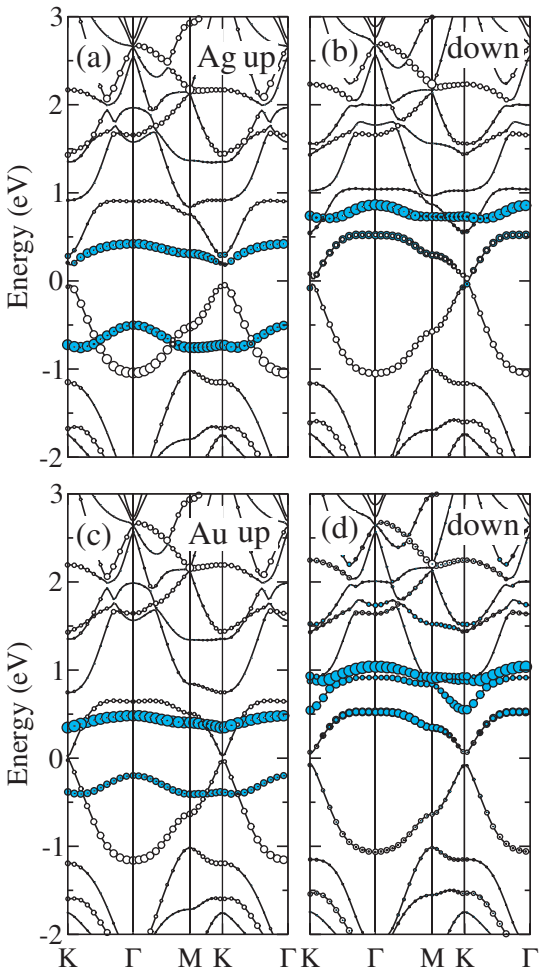

Figure 10. Similar to figure 7 for Ag and Au. The similarities with the band structure of Cu in figure 9 are evident.

Table 1 shows the distribution of the spin moment among the metal atom and the nearest carbon neighbors. We can see that the contribution from the metal atom is almost negligible, particularly in the case of Ag. This can be expected from the lower energy position of the d shell in the case of the noble metals as compared with transition metals. Although slightly hybridized with the p shell of the metal impurity, the defect states near E_F in this case are mainly coming from the carbon neighbors. Still the spin moment is rather localized in the complex formed by the metal atom and its three nearest neighbors, which for Cu and Ag contributes a

Table 3. Structural parameters and binding energies for substitutional Zn impurities in graphene for the symmetric C_{3v} and most stable distorted configurations.

	E_B (eV)	d_{C-M} (Å)	h_z (Å)	θ (°)
$Zn_{C_{3v}}$	0.91	1.99	1.67	87.9
Zn	1.07	2.06, 1.89, 1.89	1.54	88.3, 88.3, 103.9

moment of 0.83 μ_B and for Au contributes up to 0.88 μ_B. The contribution from the rest of the graphene layer is much smaller than, for example, in the case of Co. This reflects the dominant contribution from the relatively localized carbon sp lobes in the description of the defect states near E_F for these impurities. This analysis reinforces the link with the electronic structure of the unreconstructed D_{3h} carbon vacancy in graphene as presented in section 5.3. In fact, we can picture the main role of late-transition and noble-metal substitutionals in graphene as stabilizing the structure of the carbon monovacancy, which otherwise will severely reconstruct, and changing its charge state.

6. Jahn–Teller distortion of substitutional Zn

For Zn impurities, a second electron is added to the twofold degenerate E sp–d shell. Under these circumstances two scenarios are possible: (i) a non-magnetic solution in which the system has undergone a Jahn–Teller-like distortion or (ii) a high-spin solution that maintains the symmetric C_{3v} geometry of the defect. The relative energy of both solutions depends on the balance between the energy gain associated with the distortion and the exchange energy of the electrons. Both types of solutions are obtained in our DFT calculations for Zn substitutional impurities in graphene.

The details of the structure and the binding energies of the Zn impurity are presented in table 3 as calculated with SIESTA. Very similar results are obtained for both configurations using VASP. The distorted configuration presents one larger Zn–C bond (by ∼3.5%) and two shorter bonds (∼5%) compared with the bond length (1.99 Å) of the undistorted geometry. The distorted configuration is more stable by 160 meV (120 meV using VASP). This rather small energy difference between the two configurations might point to the appearance of non-adiabatic electronic effects at room temperature.

The band structure for both configurations of Zn substitutionals can be found in figure 9. Again they confirm the model presented in figure 8. The distorted Zn (figure 9(g)) breaks the degeneracy of the E sp–d levels: one of them appears fully occupied ∼0.8 eV below E_F, while the other appears a few tenths of eV above E_F. For the C_{3v} Zn impurity, both E sp–d bands are degenerate and the splitting between majority and minority levels is ∼0.71 eV. Table 1 shows the Mulliken population analysis of the spin moment for the C_{3v} Zn systems. As in the case of the noble metals, the contribution from the three nearest carbon neighbors is most important. However, the contribution of Zn is somewhat larger and the total spin moment is more delocalized with a contribution from the rest of the graphene layer of ∼0.66 μ_B. We should note that, here, we have one additional electron as compared with the noble metal systems.

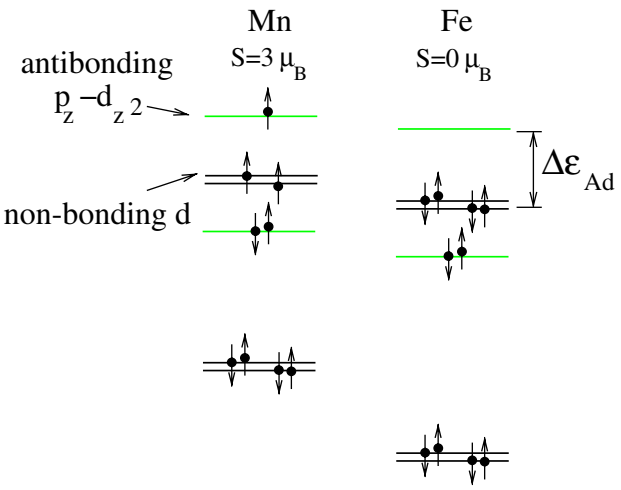

Figure 11. Scheme of the electronic levels near E_F for Mn and Fe substitutionals in graphene as deduced from our model of bonding and GGA calculations. $\Delta\epsilon_{Ad}$ is the energy cost to promote an electron to the antibonding A p_z–d_{z^2} hybridization level from the non-bonding 3d states. The magnitude of $\Delta\epsilon_{Ad}$, relative to that of the spin splitting Δ_S of these defect levels, is crucial to determine the spin state of these impurities.

7. Fe substitutionals: competition between intra-atomic interactions and metal–carbon hybridization

We have already pointed out that Fe substitutionals in graphene occupy a rather special place at the border between two well-defined regimes (see figure 3): (i) the strong 3d character of the defect levels near E_F and large spin moments found for V, Cr and Mn impurities, and (ii) the larger carbon character of those electronic levels and the small oscillatory spin moments of Co, Ni and noble metals. GGA calculations (figure 9(a)) locate Fe impurities within the second group, with all the 3d non-bonding levels fully occupied and non-magnetic. Thus, the spin moment drops from $3\,\mu_B$ for Mn impurities to zero for Fe, showing quite a discontinuous behavior as a function of the number of valence electrons. In analogy with the standard Slater–Pauling rule for transition metals, one could expect to find a more gradual decrease of the spin moment as the number of valence electrons is increased, i.e. Fe would have a moment of $2\,\mu_B$. In the present section, we study in detail why the non-magnetic solution is more stable for Fe.

7.1. Key parameters: metal–carbon hopping and intra-atomic Coulomb interactions

Figure 11 shows a scheme of the electronic structure of both Mn and Fe defects. Depending on how electrons are arranged among the A p_z–d_{z^2} antibonding level and the non-bonding 3d states, Mn can exhibit spin moments of 3 or $1\,\mu_B$, while Fe can have a moment of $2\,\mu_B$ or can be non-magnetic. At the GGA level, Mn prefers the high-spin configuration, while the low-spin one is more stable for Fe. As commented in section 5.2, the relative stability of the different spin states depends on the balance between the effects of Coulomb repulsion and exchange within the 3d levels and the relative energy position of the impurity levels given by $\Delta\epsilon_{Ad}$ (see figure 11).

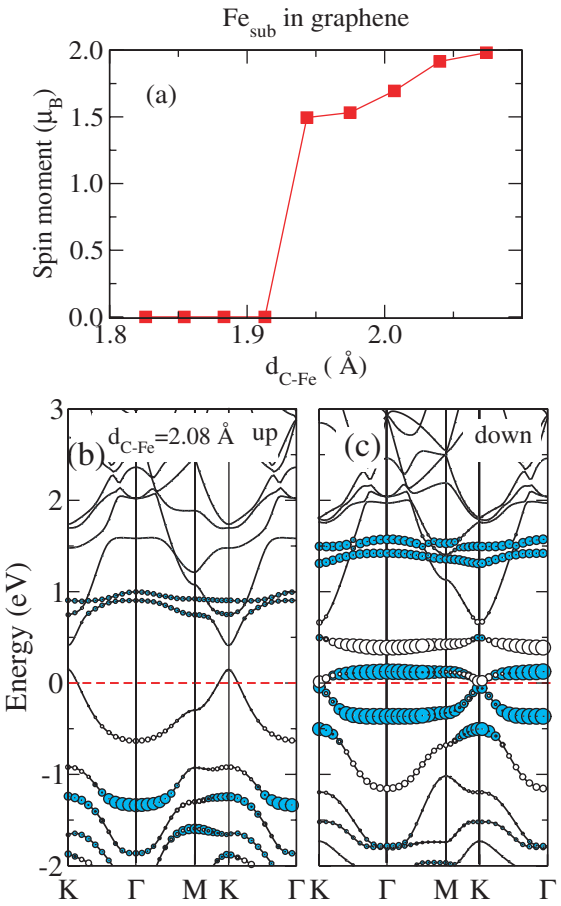

Figure 12. (a) The spin moment of a substitutional Fe impurity in graphene as a function of the C–Fe bond length. The equilibrium position corresponds to $d_{C-Fe} = 1.78$ Å. ((b) and (c)) The band structure for $d_{C-Fe} = 2.08$ Å. The symbol code is similar to that of figure 7. Energies refer to the Fermi level (indicated by a dashed line).

The hybridization with the neighboring C atoms is crucial in this interplay since it influences (i) the degree of localization of the defect levels and the screening of Coulomb interactions, which modify the spin splitting of the electronic levels Δ_S, and (ii) the value of $\Delta\epsilon_{Ad}$ through the effective hopping parameter between the 3d states and the A p_z carbon vacancy level. Next, we shall deal with both aspects for substitutional Fe in graphene.

7.1.1. Changing Fe–graphene hopping with distance. By tuning the interaction with the host structure it should be possible to change the spin moment of these impurities. We can modify the hopping by artificially changing the Fe–graphene distance. The results of such calculations are shown in figure 12(a). While maintaining the threefold symmetry of the system, we have performed a series of calculations by progressively increasing the height of the Fe atom over the graphene layer. Increasing the C–Fe bond length by ∼9% we observe an abrupt jump of the spin moment from zero to 1.5 μ_B. The spin moment continues to rise and saturates at a value of

2.0 μ_B for $d_{C-Fe} \sim 2.07$ Å. This convincingly shows that the metal–carbon hybridization is the key parameter in explaining the non-magnetic state of Fe substitutional impurity in graphene. When increasing the C–Fe distance we mainly decrease $\Delta\epsilon_{Ad}$. Thus, we reduce the energy penalty for promoting electrons from the non-bonding d to the A p_z–d_{z^2} defect levels. At the same time we also increase the atomic character of the non-bonding d states and reduce the effect of the screening due to the electrons in the graphene layer. This $\Delta\epsilon_{Ad}$ reduction promotes the electron–electron repulsion within the 3d states of Fe and, eventually, stabilizes the solution with 2.0 μ_B.

Figures 12(b) and (c) present the band structure for the high-spin state of Fe, where the C–Fe bond length has been elongated up to 2.08 Å. We note the differences with the spin-compensated ground state in figure 9(a). On the one hand, one electron is promoted from the non-bonding *d* states to the more delocalized antibonding A p_z–d_{z^2} impurity level in order to reduce the effect of electron–electron repulsion. On the other hand, the spin moment is maximized in accordance with Hund's first rule.

Therefore, we have seen that the non-magnetic character of the Fe substitutionals in the GGA calculations is due to the larger interaction with the graphene layer, as compared for example with the Mn impurity. This is consistent with the fact that Fe, together with Co and Ni, presents the smaller carbon metal bond length among the whole series of 3d transition metals. Fe impurities also have one of the largest binding energies. By artificially reducing this interaction it could be possible to obtain magnetic Fe substitutional impurities in graphene.

7.1.2. Changing intra-atomic Coulomb interaction U. Another route to explore would be to increase the size of intra-atomic electron–electron interactions. We have done so by using the so-called GGA + U methodology in which a Hubbard term is explicitly added to the DFT Hamiltonian and solved within the mean-field approximation. Our results indicate that with a reasonable value of U (∼2 eV or larger) we obtain a magnetic solution for Fe substitutionals. However, contrary to our initial expectation this solution does not correspond to the 2 μ_B high-spin solution discussed above, but to a new solution with 1 μ_B. The key factor in understanding this behavior is the partial occupation of the Fe $3d_{z^2}$ state at the level of GGA calculations. The d_{z^2} state is strongly coupled to the delocalized A p_z vacancy level appearing near E_F and both, this hybridization and the population of the atomic orbital, are strongly modified when the value of U is increased.

Figure 13 shows the results of the electronic structure of Fe impurities calculated using GGA + U with $U = 2.4$ eV and compared with those with $U = 0$. The two upper panels show the PDOS onto the d_{xy} orbital (the projection onto the $d_{x^2-y^2}$ orbital is identical by symmetry), the two middle panels show the PDOS onto the d_{z^2} orbital of Fe and the two lower panels show the total DOS. At the level of GGA, with $U = 0$, there is a very well-defined peak closely below E_F in the d_{xy} PDOS corresponding to the position of the non-bonding d states. The spectral weight coming from the d_{z^2} orbital is more spread. It presents a broad structure around −1.5 eV corresponding to the bonding A p_z–d_{z^2} defect level interacting with the valence band of graphene, as well as a narrower peak near E_F with origin in the slightly occupied antibonding A p_z–d_{z^2} impurity state. Therefore, from the Fe 3d states appearing near E_F we can picture the d_{xy} and $d_{x^2-y^2}$ states as fully occupied and the d_{z^2} as partially occupied due to the larger interaction with the carbon neighbors.

For a sufficiently large value of U the C $2p_z$–$3d_{z^2}$ hybridization is overcome by the tendency of the electrons to have an integer population within the localized 3d shell. Thus, the $3d_{z^2}$

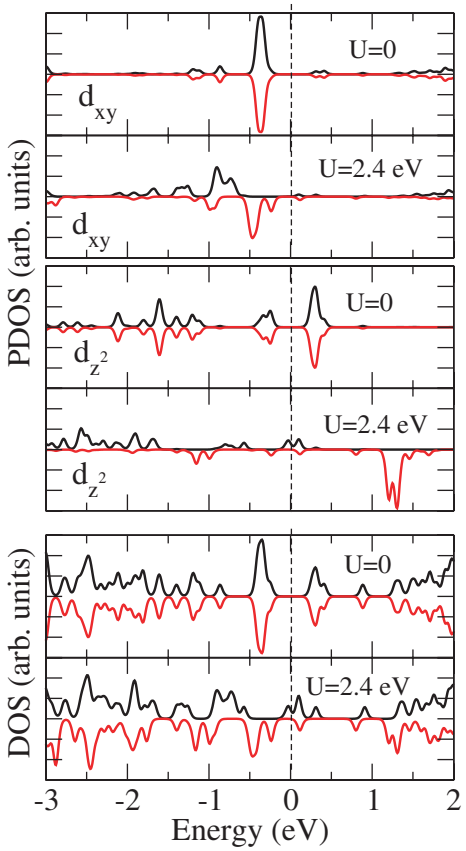

Figure 13. PDOS and total density of states (DOS) for an Fe substitutional impurity in graphene calculated with VASP using GGA and GGA + U with $U =$ 2.4 eV. Positive (negative) values for majority (minority) spin. When $U = 0$ the system shows zero spin polarization and the Fe $3d_{z^2}$ state is partially occupied. A large enough Hubbard U forces an integer population of the Fe $3d_{z^2}$ state and produces a spin moment of 1 μ_B.

localizes one electron and, as a consequence, the system develops a 1 μ_B spin polarization. These changes can be appreciated in figure 13. The majority-spin $3d_{z^2}$ PDOS shifts downwards, while a strong unoccupied peak appears around 1.5 eV in the $3d_{z^2}$ minority spin PDOS. Simultaneously, a more delocalized level mostly coming from the $2p_z$ orbitals of the neighboring C atoms appears half-filled at E_F. Note that other levels, such as the d_{xy}, do not suffer such strong modifications since they are already almost fully occupied with $U = 0$. It is also interesting to note that, due to symmetry considerations, they couple with the graphene layer very differently from the d_{z^2} level.

7.2. Relevance for recent experiments of Fe implantation in graphite

There are recent reports on the paramagnetism of iron-implanted graphite that indicate the existence of local magnetic moments associated with the implanted Fe atoms [50, 51]. This would be in contradiction with the present GGA results if we assume that the Fe atoms

are incorporated to the graphene layer as substitutionals. However, the final geometry of the implanted atoms in these experiments is not known. Furthermore, a considerable amount of defects is created during the implantation process. Although it has been argued that a large part of the damage is healed by vacancy-interstitial recombination [51], the influence of these defects, especially interstitials and big voids, on the observed magnetic response can be determinant.

Therefore, it is not fully clear if we can compare our calculations for Fe substitutional impurities in an otherwise perfect graphene layer with these experimental data. However, as we have shown in detail in this section, Fe substitutionals are very close to a transition and, depending on the details of the calculations, it is possible to obtain a magnetic ground state. In particular, Fe substitutionals develop a spin moment of 1 μ_B at the level of GGA + U calculations for reasonable values of the U parameter. This might be an indication that the non-magnetic ground state found in GGA calculations is a consequence of the limitations of the used functionals.

8. Conclusions

We have presented a DFT study of the structure, energetics and electronic and magnetic properties of several metal atoms as substitutional impurities in graphene, i.e. bound to a carbon monovacancy in the layer. We have considered the cases of all 3d transition metals, noble metals and Zn. We have paid special attention to their electronic and magnetic properties and develop a simple model for understanding the observed trends. Our model is based on the hybridization of the states of the metal atoms with those of an unreconstructed carbon vacancy. The main ingredients of the model are the assumption, after our calculations, of a threefold symmetric bonding configuration and the approximate knowledge of the relative energy positions of the levels of the carbon monovacancy and the d shell of the metal impurity as we move along the transition series. Using this model we can understand the observed variations of the electronic structure of the defect, the size and localization of the spin moment, and the binding energy. We have identified three different regimes corresponding to filling of carbon–metal hybridization shells with different character: bonding, non-bonding and antibonding.

In more detail:

(i) Most substitutional metal impurities present an almost perfectly symmetric threefold configuration with C_{3v} symmetry. Noble metals slightly depart from this perfect configuration. Only Zn presents a considerable structural distortion.

(ii) For Sc and Ti the metal–carbon bonding shell is completely filled. Therefore, these impurities present the highest binding energies and zero spin moments. Sc substitutionals act as p-dopants for graphene: each Sc impurity localizes one extra electron from the carbon layer.

(iii) The non-bonding d shell becomes partially populated for V, Cr and Mn, which develop a very localized spin moment of 1, 2 and 3 μ_B, respectively. The binding energy decreases slightly as the d shell moves to lower energies, thus reducing its hybridization with the higher carbon vacancy levels.

(iv) For Co, Ni, noble metals and Zn, the metal–carbon levels are progressively populated. This gives rise to an oscillatory behavior of the spin moment between 0 and 1 μ_B. The spin moments are more delocalized than those found for V, Cr and Mn and present a considerable contribution from the carbon atoms around the impurity. The binding energy

presents a local maximum for Co, but suddenly drops for the noble metals and has its minimum for Zn.

(v) The electronic structure, near E_F, of substitutional impurities of Co, Ni, noble metals and Zn has a strong resemblance to that of the unreconstructed D_{3h} carbon monovacancy. We can draw an analogy between the electronic structure of these impurities and that of the unreconstructed D_{3h} carbon monovacancy with different numbers of electrons (charge states). The spin moment of these impurities can be fully understood by exploiting this equivalence. In particular, the result that noble metals develop a spin moment of 1 μ_B emerges naturally within this picture.

(vi) For the Co impurity, the equivalence can be pushed a step further and we can draw an analogy with the electronic structure of a π-vacancy in a simple π-tight-binding description of graphene. This can be used to explain the peculiar behavior found for the magnetic couplings between Co substitutionals in graphene [32].

(vii) Fe impurities occupy a distinct position at the border between two different regimes. Their magnetic behavior stems from the competition between the carbon–metal hybridization and the electron–electron interaction within the 3d shell. As a result, although Fe impurities are non-magnetic at the GGA level, GGA + U calculations with moderate values of U (above $\sim$2 eV) produce a spin moment of 1 μ_B.

(viii) We have found that the unexpected result that Au substitutionals [33, 34] present a spin moment of 1 μ_B also holds for all noble metals, i.e., also Ag and Cu present a 1 μ_B spin moment.

(ix) We have found that the ground state of the Zn substitutional is non-magnetic due to a Jahn–Teller distortion. Yet, it is possible to stabilize a symmetric configuration with a spin moment of 2 μ_B with a very small energy penalty of $\sim$150 meV.

In summary, substitutional impurities of metals in graphene present some interesting magnetic and electronic properties and can therefore provide an interesting route to add functionalities or to tune the response of devices based on graphenic materials. Furthermore, recent experiments by Rodriguez-Manzo and Banhart [29] have demonstrated the possibility to create individual vacancies at desired locations in carbon nanotubes using electron beams. This ability, in combination with the high stability of substitutional impurities, can open a route to fabricate ordered arrays of these impurities at predefined locations. Such devices would allow, among other applications, the experimental verification of the theoretical predictions of unusual magnetic interactions mediated by graphene [30]–[32].

Acknowledgments

We acknowledge support from Basque Departamento de Educación and the UPV/EHU (grant no IT-366-07), the Spanish Ministerio de Educación y Ciencia (grant no FIS2007-66711-C02-02) and the ETORTEK program funded by the Basque Departamento de Industria and the Diputación Foral de Guipuzcoa. EJGS thanks N González-Lakunza for valuable help with VASP code.

Appendix. Pseudopotentials and basis orbitals radii

For the SIESTA calculations we have used Troullier–Martins norm-conserving pseudopotentials [46] generated using the pseudization radii shown in table A.1. The pseudopotentials for the

Table A.1. Cutoff radii (in Bohrs) used for the generation of the Troullier–Martins [46] norm-conserving pseudopotentials used in the SIESTA calculations. r_l stands for the cutoff radius used for the l channel, while r_{core} is the matching radius used for the construction of pseudocores in order to include nonlinear core corrections for exchange and correlation [47].

	Valence	r_{s} (a_{o})	r_{p} (a_{o})	r_{d} (a_{o})	r_{core}
Sc	$[Ar]4s^1 3d^2$	3.30	3.30	1.44	0.89
Ti	$[Ar]4s^1 3d^3$	2.96	2.96	1.45	0.72
V	$[Ar]4s^1 3d^4$	2.40	2.79	1.46	0.69
Cr	$[Ar]4s^1 3d^5$	2.51	2.80	1.46	0.65
Mn	$[Ar]4s^1 3d^6$	2.51	2.77	1.45	0.60
Fe	$[Ar]4s^1 3d^7$	2.10	2.10	1.68	0.67
Co	$[Ar]4s^2 3d^7$	2.37	2.48	1.68	0.67
Ni	$[Ar]4s^2 3d^8$	1.85	1.95	1.45	0.53
Cu	$[Ar]4s^1 3d^{10}$	2.33	2.30	1.79	0.53
Ag	$[Kr]5s^1 4d^{10}$	2.45	2.58	2.00	0.83
Au	$[Xe,4f^{14}]6s^1 5d^{10}$	2.55	2.68	2.20	0.93
Zn	$[Ar]4s^2 3d^{10}$	2.04	2.21	1.66	0.49
C	$[He]2s^2 2p^2$	1.25	1.25	1.25	–

Table A.2. Cut-off radii (in Bohrs) of the NAOs used in SIESTA as a basis set. Radii used for the s and polarization p shell are equal.

	$r_{\mathrm{sp}}^{\mathrm{NAO}}$ (a_{o})	$r_{\mathrm{d}}^{\mathrm{NAO}}$ (a_{o})
Co	8.00	4.73
Ni	10.94	6.81
Cu	8.87	5.52
Ag	10.48	6.52
Au	8.63	6.08
Zn	9.24	5.33

metal atoms include nonlinear core corrections [47] for exchange and correlation. The pseudocore radii (r_{core}) have been optimized for each element. These pseudopotentials have been tested to reproduce the correct results in bulk phases.

For most elements, the shape and radii of the basis sets of NAOs used with SIESTA were determined automatically by the code using an *energy shift* parameter of 50 meV [40, 42]. However, for some metal atoms the binding energies were slightly overestimated using these basis sets, mainly due to the confinement of the free atom. For those atoms we enlarged the radii of the basis orbitals (using smaller values of the *energy shift* parameter) until binding energies were converged within a few tens of meV. The largest radius for each element and l channel is shown in table A.2. Note that the DZP basis of these metals includes a p shell. In this case, the radii of p orbitals are taken to be equal to that of the s shell.

References

[1] Geim A K and Novoselov K S 2007 *Nat. Mater* **6** 183
[2] Castro Neto A H, Guinea F, Peres N M, Novoselov K S and Geim A K 2009 *Rev. Mod. Phys.* **81** 109
[3] Novoselov K S *et al* 2005 *Nature* **438** 197
[4] Katsnelson M I, Novoselov K S and Geim A K 2006 *Nat. Phys.* **2** 620
[5] Park C, Son Y W, Cohen M L and Louie S G 2008 *Nat. Phys.* **4** 213
[6] Avouris P, Chen Z and Perebeinos V 2007 *Nat. Nanotechnol.* **2** 605
[7] Hueso L E *et al* 2007 *Nature* **445** 410
[8] Trauzettel B *et al* 2007 *Nat. Phys.* **3** 192
[9] Tombros N, Jozsa C, Popinciuc M, Jonkman H T and van Wees B J 2007 *Nature* **448** 571
[10] Yazyev O V 2008 *Nano Lett.* **8** 1011
[11] Fischer J, Trauzettel B and Loss D 2009 *Phys. Rev.* B **80** 155401
[12] Son Y W, Cohen M L and Louie S G 2006 *Nature* **444** 347
[13] Mañanes A, Duque F, Ayuela A, López M J and Alonso J A 2008 *Phys. Rev.* B **78** 035432
[14] Yazyev O V and Katsnelson M I 2008 *Phys. Rev. Lett.* **100** 047209
[15] Esquinazi P, Spemann D, Höhne D, Setzer A, Han K H and Butz T 2003 *Phys. Rev. Lett.* **91** 227201
[16] Lehtinen P O, Foster A S, Ayuela A, Krasheninnikov A V, Nordlund K and Nieminen R 2003 *Phys. Rev. Lett.* **91** 017202
[17] Lehtinen P O, Foster A S, Ma Y, Krasheninnikov A V and Nieminen R 2004 *Phys. Rev. Lett.* **93** 187202
[18] Makarova T and Palacios F (ed) 2006 *Carbon Based Magnetism* (Amsterdam: Elsevier)
[19] Krasheninnikov A V and Banhart F 2007 *Nat. Mater* **6** 723
[20] Uchoa B, Kotov V N, Peres N M R and Castro Neto A H 2008 *Phys. Rev. Lett.* **101** 026805
[21] Yazyev O V 2008 *Phys. Rev. Lett.* **101** 037203
[22] Palacios J J, Fernández-Rossier J and Brey L 2008 *Phys. Rev.* B **77** 195428
[23] Fernández-Rossier J and Palacios J J 2007 *Phys. Rev. Lett.* **99** 177204
[24] Gan Y, Sun L and Banhart F 2008 *Small* **4** 587
[25] Ushiro M, Uno K, Fujikawa T, Sato Y, Tohji K, Watari F, Chun W J, Koike Y and Asakura K 2006 *Phys. Rev.* B **73** 144103
[26] Santos E J G, Ayuela A, Fagan S B, Mendes Filho J, Azevedo D L, Souza Filho A G and Sánchez-Portal D 2008 *Phys. Rev.* B **78** 195420
[27] Banhart F, Charlier J C and Ajayan P M 2000 *Phys. Rev. Lett.* **84** 686
[28] Dresselhaus M S, Dresselhaus G and Avouris P 2001 *Carbon Nanotubes: Synthesis, Structure, Properties and Applications* (Berlin: Springer)
[29] Rodriguez-Manzo J A and Banhart F 2009 *Nano Lett.* **9** 2285
[30] Brey L, Fertig H A and Das Sarma S 2007 *Phys. Rev. Lett.* **99** 116802
[31] Kirwan D F, Rocha C G, Costa A T and Ferreira M S 2008 *Phys. Rev.* B **77** 085432
[32] Santos E J G, Sánchez-Portal D and Ayuela A 2010 *Phys. Rev.* B **81** 125433
[33] Krasheninnikov A V, Lehtinen P O, Foster A S, PyykköP and Nieminen R M 2009 *Phys. Rev. Lett.* **102** 126807
[34] Malola S, Häkkinen H and Koskinen P 2009 *Appl. Phys. Lett.* **94** 043106
[35] Boukhalov D W and Katsnelson M I 2009 *Appl. Phys. Lett.* **95** 023109
[36] Suarez-Martinez I and Ewels C P 2009 private communication
[37] Perdew J P, Burke K and Ernzerhof M 1996 *Phys. Rev. Lett.* **77** 3865
[38] Venezuela P, Muniz R B, Costa A T, Edwards D M, Power S R and Ferreira M S 2009 *Phys. Rev.* B **80** 241413
[39] Sánchez-Portal D, Ordejón P, Artacho E and Soler J M 1997 *Int. J. Quantum Chem.* **65** 453
[40] Soler J M, Artacho E, Gale J D, García A, Junquera J, Ordejón P and Sánchez-Portal D 2002 *J. Phys.: Condens. Matter* **14** 2745
[41] Sánchez-Portal D, Ordejón P and Canadell E 2004 *Principles and Applications of Density functional Theory in Inorganic Chemistry II (Structure and Bonding Series, vol 113)* (Berlin: Springer) pp 103–170

[42] Junquera J, Paz O, Sánchez-Portal D and Artacho E 2001 *Phys. Rev.* B **64** 235111
[43] Kresse G and Hafner J 1993 *Phys. Rev.* B **47** 558
[44] Kresse G and Furthmüller J 1996 *Phys. Rev.* B **54** 11169
[45] Monkhosrt H J and Pack J D 1976 *Phys. Rev.* B **13** 5188
[46] Troullier N and Martins J L 1991 *Phys. Rev.* B **43** 1993
[47] Louie S G, Froyen S and Cohen M L 1982 *Phys. Rev.* B **26** 1738
[48] Dudarev S L, Botton G A, Savrasov S Y, Humphreys C J and Sutton A P 1998 *Phys. Rev.* B **57** 1505
[49] Sánchez-Portal D, Santos E J G and Ayuela A 2009 submitted
[50] Sielemann R, Kobayashi Y, Yoshida Y, Gunnlaugsson H P and Weyer G 2008 *Phys. Rev. Lett.* **101** 137206
[51] Barzola-Quiquia J, Höhne R, Rothermel M, Setzer A, Esquinazi P and Heera V 2008 *Eur. Phys. J* B **61** 127